Transport Properties of Electrons in Silicon Drift Detectors measured in Large Magnetic Fields.

S.U. Pandey, D. Cooper, H. Dyke, D. Elliot, T.J. Humanic, J. Kirkman, I.V. Kotov, G. Lo Curto, E. Sugarbaker, G. Vilkelis
The Ohio State University, Columbus, OH 43210, USA.

R. Bellwied, L. Dou, A. French, J. Hall, C. Pruneau, V. Rykov, J. Takahashi, W.K. Wilson
Wayne State University, Detroit, MI 48201, USA.

R. Beuttenmueller, W. Chen, D. DiMassimo, H.W. Kraner, C.J. Liaw, D. Lynn, J. Sedlmeir
Brookhaven National Laboratory, Upton, NY 11973, USA.

G.W. Hoffmann, S. Paganis, D. Read, J. Schambach
University of Texas, Austin, TX 78712, USA.

Abstract

A 45x45 mm rectangular n-type Silicon Drift Detector was studied in magnetic fields ranging from 0 to 4.7 T and for drift fields from 200 to 380 V/cm. Transport properties of electrons in silicon (Hall mobility, drift mobility and magnetoresistance) were determined by pulsing the detector with a Nd:Yag laser at different drift lengths and measuring both the transverse deflections of the signal and the increases in drift time versus an applied magnetic field. The width of the signal in both the drift and anode direction increased with magnetic field. The magnetic field was aligned parallel and normal to the the drift direction. The detector was found to operate well for conditions expected in future experiments at the RHIC collider and experiment E896 at Brookhaven National Laboratory.

(to be submitted to Nuclear Instruments and Methods)

1 Introduction

A Silicon Drift Detector (SDD) is a charged particle position measuring device with a position resolution on the order of 10 μm in each coordinate[1, 2, 3]. A charged particle crossing the detector leaves a trail of electron-hole pairs along its path. Holes are immediately absorbed by the cathodes on the surface of the detector. Electrons converge to the middle of the bulk and drift at a constant speed under the influence of an applied uniform electric field (E) toward low capacitance anodes located near the edge of the silicon wafer. One coordinate of the particle position is determined from the drift time while charge division between anodes gives the other coordinate.

Future experiments will take place in high luminosity machines such as the Large Hadron Collider (LHC), the Relativistic Heavy Ion Collider (RHIC), and experiment E896 at the Alternating Gradient Synchrotron (AGS) where magnetic fields up to 7 T are present. Silicon detectors are expected to track charged particles often under high magnetic fields for momentum measurements. Thus the ability of these detectors to work under such conditions is important to study.

The goal of this present work is to apply large magnetic fields (B) (up to 4.7 T) to a prototype STAR SDD (designated "STAR-1") to determine whether it still functions under these conditions and to investigate the motion of charge carriers in the SDD under such B fields. The Hall mobility, drift mobility, and their ratio, the Hall factor (r_h), were determined by pulsing the detector with a Nd:Yag laser at two different drift lengths and measuring both the transverse deflection of the signal and the increase in drift time versus the applied B field.

2 Background

The measurements were made using a STAR-1 4.5 cm x 4.5 cm rectangular, 300 μm thick, one-way drift SDD's having 178 anodes at 250 μm pitch and 332 cathodes at 120 μm pitch. They were made out of 3" diameter 8 k$\Omega\cdot$cm N-type NTD Silicon wafers with (111) crystal orientation. Fig. 1 shows a schematic diagram of a STAR-1 detector. The operation of the detector has been described in detail elsewhere[4].

A minimum ionizing particle deposits about 25000 electrons. These electrons are constrained to the center of the silicon wafer while they drift towards the anodes subject to diffusion and coulomb self-repulsion producing an approximately gaussian spread in carrier density[5]. A B field parallel to the drift direction, x, affects the dynamics of electron transport in the SDD initially when the electrons are swept to the center of the wafer along the ionization path and just before collection at the anodes when the electron cloud is swept up towards the surface of the wafer. Longitudinal magnetoresistance, discussed below, can lower the drift velocity in this configuration. A B field perpendicular to the drift direction but parallel to the wafer surface, y, causes a force perpendicular to the wafer but the constraining parabolic depletion voltage potential limits this motion. The depth of the parabolic valley is about 10 V over 150 μm, and a typical drift velocity in this experiment is $v_d \approx 4\mu m/ns$ hence the ratio of the Lorentz forces $\vec{E}/(\vec{v} \times \vec{B})$ is large. The electron cloud drifts towards the anodes a few microns above the center of the wafer. Unlike standard Hall experiments this does not give rise to opposing electric fields from charge (hole) accumulation on the wafer surface as cathode strips on the surface collect and transport charge away. A B field perpendicular to the drift direction and the wafer surface, z, causes motion in the plane of the wafer. The electron cloud is swept laterally towards neighboring anodes.

Solutions to the differential equations of motion are well known for single electrons[6] when the average kinetic energy of the electron from external forces is of the same order as the thermal kinetic energy and the effect of collisions is modelled by an additional force proportional to the velocity. Particles move at a constant velocity proportional to the forces on them. Lorentz forces give rise to two perpendicular and constant forces and the motion of an electron is a straight line. The velocity along the drift direction, v_x, and perpendicular to it but parallel to the wafer, v_y, are modified as follows:

$$v_x = \frac{\mu_d^0 E_x}{1+\mu_h^2 B_z^2} = \frac{v_x^{noB}}{1+\mu_h^2 B_z^2} \tag{1}$$

$$v_y = \mu_h B_z v_x \tag{2}$$

where μ_d^0 is the drift mobility in the absence of a B field, μ_h is the Hall mobility, and B_z the magnetic field transverse to the drift. Note that v_x is reduced by $(1+\mu_h^2 B_z^2)$ as B_z increases. From eq. (2) the transverse deflection is

$$y = \mu_h B_z L \tag{3}$$

where L is the distance to the anodes from the ionization point. This is true independent of changes in μ_d. From eq. (1) the drift time increases as

$$t_B = t_{noB}(1 + \mu_h^2 B_z^2) \tag{4}$$

However, a more precise solution arises when the Boltzmann equation is solved in the Lorentz model to powers of B beyond the first, and it is found that the conductance decreases as B^2 (with smaller higher order terms in B). This behavior is well documented in experiments[7, 8, 9] for $B < 15$ T and was first predicted over 100 years ago[10]. Further, since a reversal of B field should cause the same behavior, this effect must be proportional to B^2 on symmetry grounds. A naive explanation for this phenomena is that when a B field is introduced, path trajectories become helices for the periods of time between successive collisions, causing an increase in path length. While this decrease in conductance is maximal for B fields perpendicular to the drift (transverse magnetoresistance or TM) it also exists to a lesser degree for B fields parallel to the drift (longitudinal magnetoresistance or LM). The latter behavior (LM) arises from non-spherical Fermi surfaces leading to anisotropies in the tensor of effective mass or scattering time[8] and can lead to both larger or smaller dependences of the conductance on B^2. Probing the magnetoresistance behavior of a substance can reveal details of how electrons are distributed as functions of energy and wave vectors in the bands of a solid.

Since conductance is proportional to drift mobility these ideas can be roughly expressed for TM as $\Delta\mu_d/\mu_d = -a^2 B_{y,z}^2$ or $\mu_d = \mu_d^0/(1 + a^2 B_{y,z}^2)$ and for LM as $\mu_d = \mu_d^0/(1 + b^2 B_x^2 p)$ where a and b are constants, $p = 1$ assumes a B^2 dependance for LM, and $B_{y,z}$ is the B field transverse to the drift, and B_x is the B field parallel to the drift. Note that for the setup we use in our experiment (see Section 3) $B_x^2 = (4.7T)^2 - B_{y,z}^2$. Therefore, as the TM gets larger the LM gets smaller in this experiment. Usually the TM is stronger than the LM. Identifying $t_{noB} = L/\mu_d^0 E_x$ leads to a modified eq. (4)

$$t_B = t_{noB}(1 + \mu_h^2 B_{y,z}^2)(1 + a^2 B_{y,z}^2)(1 + b^2((4.7T)^2 - B_{y,z}^2)^p) \tag{5}$$

where p is usually 1. After collecting terms and defining new constants c, d, e, and f

$$t_B = t_{noB}(1 + c^2 + d^2 B_{y,z}^2 + eB_{y,z}^3 + fB_{y,z}^4) \approx t_{noB}(1 + c^2 + d^2 B_{y,z}^2) \tag{6}$$

where $eB^3_{y,z}$ and $fB^4_{y,z}$ can be negative and are expected to be quite small for the B fields in this experiment, and the constant $c^2 = b^2 \cdot (4.7T)^2$. Note that the drift time inside the magnet with the field parallel to the drift ($B_{y,z} = 0$) increases by $1 + c^2$ from the drift time outside the magnet. The same functional form can be used to fit eq. (4) as eq. (6), since constants e and f are small. Since $d = f(a, b, \mu)$ is a complicated function no attempt is made to determine a^2 or μ_h^2 from d^2 and d can be thought of as an effective mobility. It should be emphasized that eq. (6) is only true for the particular geometry applied in this experiment.

The ratio of μ_h/μ_d^0 or the Hall mobility to the drift mobility is the Hall factor, r_h. The ratio differs from 1 primarily due to scattering mechanisms in silicon and how the free time between collisions varies with electron energy. When scattering by ionized flaws is large the ratio can exceed 1.9 and when constant energy surfaces for an electron are perturbed significantly from a spherical form the ratio can be as low as 0.7[8]. For n-type material r_h is expected to be largely independent of temperature[11, 12] in the range of temperatures ($13 - 18\ ^\circ C$) sampled in this experiment and is presented in this paper. Usually there is a slight increase in r_h with temperature (less than 1% for our temperature range). As only electrons drift in our detector we only present r_h for electrons, not for holes.

3 Experimental Procedure

Measurements were carried out at The Ohio State University Silicon Detector Test Laboratory and the The Ohio State University Magnetic Resonance Imaging Laboratory.

Nonmagnetic materials were used wherever possible in the experiment setup. The detector was mounted on a plastic board from which connections were made to the anode preamplifiers and to all external voltages. In addition, a temperature probe was placed beside the detector. The plastic board was attached to a wooden cylindrical support, which could be pushed into a superconducting magnet. Fig. 1 shows a schematic diagram of the setup.

A General Electric superconducting magnet provides a 4.7 T field along its solenoid axis within a 25 cm diameter hole. It is highly uniform 80 cm from the bore edge as seen in fig. 2, where measurements were carried out by observing the shift in the resonant frequency of H^1 in the NMR spectrum[13].

The maximum deviation of the field in a 10 cm^3 cube is 0.0004% of 4.7 T. For each measurement the detector was positioned 80 cm from the bore edge in z and at the center of the hole. Components of the B field normal to the drift direction could be changed by rotating the detector in θ as seen in fig. 1. Systematic errors were checked by rotating the detector by 180° in the azimuth with respect to the solenoid axis.

Charged particle events were simulated using a Nd:YAG laser of wavelength 1.064 μm, just above the band edge where silicon becomes transparent. The laser pulse duration was 8 ns. The size of the laser spot on the surface was about 150 μm which does not introduce significant additional uncertainty in the drift position since it is smaller than the natural charge cloud spread ($\approx 250\mu$m) due to coulomb self-repulsion and diffusion and it does not affect the mean of the drift cloud position. The laser was placed about 15 m away from the magnet. A photo-diode with a 500 ps rise time positioned in front of the laser provided a trigger. The laser light was delivered by a 100 μm thick optical fiber attached to a movable x-y support fixed about 0.5 mm above the surface of the wafer. The position of the movable x-y support was determined via a micrometer. The detector electronics were pulsed by external electronics to check their operation.

The external voltage divider board was placed 5 m from the magnet bore hole. Flat cables carried the high voltage to the detector. Although a twisted pair cable carried the voltages that focussed the electron cloud onto the anodes, this cable was the major contribution to noise in the experiment. For this particular setup a high pass filter at the detector might have reduced this noise but was not implemented as the signal was clearly visible. Twisted pair cables carried signals approximately 8 m from the preamps to gaussian shapers. These shapers were readout via digitizing oscilloscopes (10 ns/point). The signals from seven neighboring anodes were transferred via a GPIB bus to a Macintosh computer running Labview. Twenty triggers were acquired and stored for each orientation of the B field with respect to the detector. The temperature was readout and stored with the waveforms.

Three drift fields of 200 V/cm, 267 V/cm, and 378 V/cm were used in all three orientations of the B field with respect to the drift direction. Data were taken both inside and outside the region of high B field. The laser amplitude was attenuated to deposit the same amount of energy as 2-3 times the energy of a minimum ionizing particle to improve the signal to noise ratio. The calibration was done using a ^{234}Pa source (E_β=2.29 MeV), however, the laser has 20% pulse-to-pulse amplitude fluctuations. Data were taken for laser events at distances of 1.3 $\pm$ 0.3 mm and 25 $\pm$ 1 mm from the anodes. The large errors arise from uncertainties in the position of zero and from slight nonlinearities in the drift field for this setup.

As B_z increases so does the lateral deflection as seen from eq (3). Instead of reading out different anodes for each new setting, the same anodes were read out to minimize gain variations (all seven anode channels have nearly identical gains) and detector handling. This required that the optical fiber carrying the laser signal be occasionally moved. For the 1.3 mm measurement only two such changes were necessary since the lateral displacement was small between successive B_z increments (2-3 anodes). The displacement of the optical fiber was calibrated by comparing the signals on the 7 anodes for the same B_z. Errors in the displacement of the optical fiber were hence small. The error in anode position was estimated to be 25 μm, arising primarily from signal to noise ratios when estimating coordinates via charge division along the anodes as well as systematic uncertainties from handling the detector. For the 25 mm measurement, calibration of the displacement of the optical fiber for successive B_z increments via looking at the signal on the anodes for the same B_z was not possible as the typical displacement per field increment was 20 anodes. A conservative systematic error was convoluted with the charge division error to give 350 μm, which is still small compared to the total displacement (20 x 250 μm/anode) per B_z increment. It should be noted that most anodes have similar leakage currents as seen in fig. 3. Thus the potential well under each anode is thought to be of the same depth and should not add to the error in anode determination[14].

Measurements were made about one to two minutes after the detector had been placed in the magnet. This allowed eddy currents in the detector and surrounding electronics to subside. After each measurement the wooden structure was taken out and then reinserted after the detector orientation had been changed. This handling resulted in position determination errors mentioned above.

4 Data and Results

A typical waveform is shown in fig. 4a. The signal is clearly visible superimposed on a large background. It should be noted that the signals presented in the literature[15] are usually much cleaner. While drift times, anodes hit, and widths of the cloud can be determined from this raw signal, some preprocessing of the data were tried as well and the results are shown in fig. 4b.

A Parzen[16] window was used to minimize spectral leakage and a moving average was used to reduce variances when the power spectrum of the data were estimated using the Fast Fourier Transform (FFT). The results are shown in fig. 5. Since we digitized the data in 10 ns bins and expect to see gross signal characteristics only on the scale of a few bins we expect the signal to be confined to below 10 MHz. However, there is also a low frequency component which is below 0.5 MHz as seen from fig. 4a. We created an optimal Wiener filter[16] to reduce the noise. Hard cuts on high and low frequency components of the power spectrum lead to similar results. The data were deconvoluted with information taken with a delta function input to the anodes. The data are then taken back to the time domain via a inverse FFT.

A clearer estimate of the power spectrum can be obtained from maximum entropy methods as seen in fig. 5c. This estimator uses the complex frequency plane and is sensitive to poles in distributions[16]. This estimator resolves the noise spectrum of the data, however, all phase information in the FFT is lost and thus while an inverse FFT is not possible this method allows the contruction of a better Wiener filter. Wavelets[16] can be used instead of an FFT. This method allows sensitivity to both fine and large scale features of the data but it was difficult to construct good noise filters with them. While the different techniques clean up the data to different degrees the position and width of the peak do not vary significantly with the techniques. Further, we are interested in relative changes with the B field, and each method shows consistent trends in the data. Thus these methods were not used in this paper but show the robustness of the results to the preprocessing of the data.

Data were taken at 13 to 18 $°C$ and were normalized to 14 $°C$. The normalization was done from the curve in fig. 3. While the absolute temperature of the wafer might not be known, the change in the drift time with temperature is easily measurable and follows the theoretical dependence of $T^{2.5}$[3, 6]. Also shown in fig. 3 is the anode leakage current which is seen to drop with temperature and is fairly constant across the anodes. Most of the data were taken at 14 $°C$ where the detector operates better due to smaller anode leakage currents.

Drift times change by a few ns from anode to anode, in one pulse, due to the longer time needed to travel to a neighboring anode (250 μm/anode = Δ). The drift time for each pulse was estimated at the anode with the largest signal. The sigma along the drift direction was determined by a gaussian fit to the data. To determine which anode was hit a simple charge sharing algorithm was used. This was checked with a gaussian fit to the data. The width along the anode direction was difficult to measure as usually only three anodes had appreciable response (Q_i). A combination of moments analysis, $\sigma = \Delta ln^{-0.5}(Q_2^2/Q_1Q_3)$, and gaussian fits were used to extract the sigma. Finally, the measured sigma, σ_m, was related to the actual sigma, σ_a, via $\sigma_m^2 = \sigma_a^2 + \Delta^2/12$. Errors include systematic uncertainties.

Estimates of the Hall mobility for electrons can be obtained from the lateral position deflections presented in fig. 6. In principle the Hall mobility can also be calculated from the change in drift time with B_z and from the increase in the width of the electron cloud with B_z. This was not done in the former case due to difficulties in extracting μ_h from the data (see Section 2) and in the latter case due to large errors in determining the cloud width in the measurements. The data were fit with MINUIT[17], a powerful and flexible minimization library package. Standard χ^2 minimization fits were performed and the statistic minimized for linear fits to eq. (3) was:

$$\chi^2 = \sum_i \frac{(y_i - \alpha - \mu_h L B_i)^2}{\sigma_{y_i}^2 + \mu_h^2 L^2 \sigma_{B_i}^2} \tag{7}$$

where y is the lateral deflection, L is the distance to the anodes from the ionization point, α is the $B_z = 0$ intercept, and σ_y and σ_B are the errors in determining y and B_z. The drift time data were fit to the same functional form as eq. (4) and the statistic minimized was:

$$\chi^2 = \sum_i \frac{(t_{B_i} - \alpha(1 + d^2 B_i^2))^2}{\sigma_{t_{B_i}}^2 + 4\alpha^2 d^4 B_i^2 \sigma_{B_i}^2} \tag{8}$$

where t_B is the drift time, α is the $B_z = 0$ intercept, σ_{t_B} and σ_B are the errors in determining t_B and B_z, and d is a complicated mixture of magnetoresistance coefficients and μ_h (eq. (6)) and can be thought of as an effective mobility. This effective mobility is unique to this experimental setup. As the detector was pushed in and out of the magnet it moved by a maximum of 3° in θ (see fig. 1) causing an uncertainty in the applied B_z.

System	Hall Factor
25 mm Drift 267 V/cm	1.6 ± 0.2
1.3 mm Drift 267 V/cm	1.4 ± 0.3
1.3 mm Drift 378 V/cm	1.4 ± 0.3

Table 1: The Hall Factor for different configurations calculated from the lateral deflection of the electron cloud with B field. Errors are statistical plus systematic.

To calculate the Hall factor the drift mobility must be known. A measurement was taken outside the magnet ($B = 0$) of the drift time versus the position for two known drift fields and the drift mobility calculated from the slope or velocity divided by the drift field. Both values were found to be $(0.157 \pm 0.004)\ m^2/(V \cdot s)$. This is slightly higher than values quoted in the literature[6] perhaps due to defects in the silicon crystal structure. The drift data was fit for the effective mobility using eq. (8), and it was found to be 76% of the drift mobility outside the magnet due to magnetoresistance. The data and fits can be seen in fig. 7. Note that the same effective mobility is used for all plots in fig. 7.

The Hall mobility normalized to the drift mobility (the Hall factor, r_h) to minimize temperature dependences are presented in Table 1 for both drift distances and each drift field. A large component of the error for measurements of r_h from the lateral deflection come from uncertainties in the distance from the anodes, L in eq. (3). As seen the values of r_h are consistent for all measurements and averaging the measurements we obtain 1.5 ± 0.1 for r_h. Variations of the Hall mobility with B field were not studied as they were felt to be beyond the precision of this experiment. The data are seen together with the fits in fig. 6. The χ^2 per degree of freedom was close to 1 for all fits.

The width of the signal increases with B_z in both the drift and anode directions, though the latter have large uncertainties. This increase could arise since carriers which do not travel along the longitidunal direction of a momentum valley of an energy ellipsoid in the wafer are subject to forces that can give rise to a transverse component of the current density resulting in spreading of the cloud[18]. A more likely cause is the increase in drift time with B_z (see eq. (6)). It is known that

$$\sigma_c = \sqrt{2Dt} \tag{9}$$

where D is the electron diffusion constant, σ_c is the cloud width in units of distance, and t the drift time. To convert σ_c to time one divides by the drift velocity. eq. (6) and eq. (9) detail how the drift time and signal width increases with B_z and the results are shown plotted in fig. 7. Note the good agreement between the data and the fit using the effective mobility from eq. (6). The signal shape did not show any additional skewness with applied B_z indicating the magnetoresistance does not cause large distortions in the transport properties of the electron cloud for these B fields. Further, it would appear that magnetic breakdown, which occurs when the cyclotron frequency is larger than the band gap, is not a problem, since the detector behaved as expected as B_z was increased.

The drift time changes when the detector is aligned with the B field parallel to the drift compared to the $B = 0$ case. We know that $B_{y,z} = 0$ as there is no change in the lateral deflection when the detector is put into the magnet. This change in the drift time is thought to be the result of longitudinal magnetoresistance (LM). The coefficient of LM can be estimated from the increase in drift time of the detector placed inside the magnet as compared to outside (eq. (6)). For both the 200 V/cm at 1.3 mm and the 267 V/cm at 25 mm the data show the same percent increase of 12.5 ± 0.5 implying that $\Delta\mu_d/\mu_d = (-5.7 \pm .2)\ 10^{-3} B^2$ (B in T), if one assumes a B^2 dependance. When the B field is oriented perpendicular to the drift but parallel to the wafer, y, an increase is seen in the drift time inside the magnet compared to the $B = 0$ case. Here it is thought to be due to transverse magnetoresistance (TM). For data at 200 V/cm and 378 V/cm taken at 25 mm the percent increase in drift time is 20 ± 1 implying that $\Delta\mu_d/\mu_d = (-9.1 \pm 0.5)\ 10^{-3} B^2$, ($B$ in T). The TM contribution is larger than the LM as expected. The ratio of TM to LM is 1.6 ± 0.1. Like r_h this number reflects the magnitudes of different scattering mechanisms and the details of the band structure within silicon. In the literature[19, 20] for (1,1,1) n-type silicon albeit at a different B field (1.0 T) the value of TM is a factor of 2 larger than we measured. In reference[20] LM is equal to the value we measure. The authors of this reference[20] made their measurements at much higher drift fields and note that their results depend on the drift field. Our experiment had a relatively limited coverage of drift field so this could not be confirmed. However, differences between the measurements most likely arise due to the different purity silicon used in our experiment and the different B fields. Note further that around 0.5 T in B_z there is a decrease in the drift time seen in the 267 V/cm data at both drift distances (see fig. 7) and in the 378 V/cm data at 1.3 mm. This decrease is at the 1% level and could be a systematic error or reflect very strong and nonlinear deviations of the magnetoresistance with B[21]. It could also arise from a minima in the dependance of r_h on the B field[22, 23].

The electron cloud still drifts as expected when the B field is perpendicular to the drift but parallel to the wafer, y. The parabolic constraining field is much larger than the perpendicular force arising from the B_y field. Large nonhomogeneous fields in experiment E896 will cause the SDD to experience such B fields. It was not possible to change B_y for this configuration by any rotation. Further, as mentioned above, the drift time increased with B_y compared to the $B = 0$ case. The amplitude of the signal showed no systematic change when inserted into the B field and increased with drift field as expected since faster drift times means less spreading of the electron cloud. For low drift fields, 200 V/cm, it was possible to drift in this configuration, however, when $B_y = 0$ and $B_z > 0.5$ T the signal stoped drifting.

Several data sets were taken at a constant B_z but different drift fields. These serve as checks on systematic errors on the above measurements. The transverse deflection is independent of the drift field as expected and seen in fig. 8. The drift times and cloud width's decrease with increasing drift fields as $1/E$ as expected. The ratio of the slopes for fig. 8a and fig. 8c should correspond to the ratio of the coefficients of TM to LM and is 1.4 and the ratio of the slopes in fig. 8c to fig. 8e is equal to the ratio of the two drift distances within errors. However, due to limited statistics and large χ^2 of the fits these numbers have wide confidence limits associated with them and should only act as indicators.

Finally, to simulate a magnet quench, the detector was pushed into the magnet within two seconds. Magnet quenches in experiment E896 are expected to take ten seconds. No deviations from previous measurements were observed in this case.

5 Discussion

The SDD has been shown to work with respect to all orientations of large B fields. Potential concerns such as glue that is magnetic, preamplifier failure, or large eddy currents causing bonds to break have been shown to be unwarranted. An increase in the drift time occurs when it is put into the B

field, even when the field is parallel to the drift. This is thought to be due to transverse and longitudinal magneteoresistance. A measurement of coefficients of each of these quantities is presented, and LM found to be smaller than TM as expected. For LM the functional form of B^2 was assumed but it could be B^4 which would make LM even smaller. One should note that the increase in drift time with B_z is only clearly evident above 1 T, a region not explored by previous experiments.

It is observed that the B field did not affect the standard operation of the detector in the sensitive area around the anodes where the voltages are adjusted to force the electron cloud to drift to the anodes on the surface of the wafer. No significant distortions were seen in the shape or amplitude of the signal with increasing B field in any orientation with respect to the drift. However, in the B field, the electron cloud stopped drifting at lower drift fields (< 200 V/cm) when $B_y = 0$ and $B_z > 0.5$ T. This could be due to the sensitive nature of the anode area to external forces. As such low drift fields will not be used in experiment E896 at the AGS and in STAR at RHIC, this is not a problem for these experiments.

This experiment has demonstrated a new method to measure r_h. In principle experiments of this type can give much higher precision measurements of r_h but due to uncertainties in the drift distance to the anodes in this experiment errors are relatively large. Experiments with greater accuracy can be done in the future to map out any changes in r_h with B and drift field. Further, more precise steps in B might enable one to deduce information about the structure of Fermi surfaces in the material.

Previous measurements of r_h have worked with low values of B, typically under 0.5 T, and have found values around 1.2 to 1.3 [24, 25, 22, 26]. These measurements were made for n-type silicon of different purity, homogeneity, resistivity, different orientations of the B field with respect to the crystallographic axis, and assumed values of the drift mobility from different experiments. It is known that r_h depends on all these variables and they can lead to variations up to a factor of two[8, 21, 23]. We measure $r_h = 1.5 \pm 0.1$. Also it should be emphasized that in this experiment both the drift mobility and the Hall mobility were measured.

As seen in fig. 7 the sigma of the signal in the drift direction increases quite significantly with the B field. The detector will perform adequately at RHIC for experiment STAR where fields of 0.5 T are expected. For experiment E896 (which will run in the fall of 1996 at BNL) where fields up to 7 T are expected there will be a degradation of the two track resolution due to increased width of the signal by almost a factor of 2. However, due to low expected occupancies in these detectors this is not foreseen to be a problem. In STAR and E896 the B fields are oriented in directions such that the effective dead area (lack of coverage) does not change with B. If B fields perpendicular to the wafer and drift exist, then part of one edge far from the anodes will be lost as the electron cloud is swept out of the detector. Further, each detector for E896 will have to be calibrated for drift time at a known distance at the B field it sits in due to the effects of magnetoresistance changing the effective drift mobility.

6 Conclusions

It was shown that Silicon Drift Detectors work well in large magnetic fields (up to 4.7 T). They can be used as a new method to measure the Hall factor. They can also be used to investigate the longitudinal and transverse magneteoresistance properties of silicon. The width of the signal from the Silicon Drift Detector increases with transverse magnetic fields at a fixed distance from the anodes. While this leads to a slight degradation of the two track resolution the detector will work well for experiments STAR at RHIC and E896 at BNL. Finally, the detector can survive a magnet quench from 5 T increasing its ease of use in E896.

7 Acknowledgements

We thank the technical staff at The Ohio State University Magnetic Resonance Laboratory, in particular Professor Pierre-Marie Robitaille for providing access and Dr. Dipti Rath for technical guidance in the use of the magnet. We are also grateful for the partial support given by the US Department of Energy through grant DE-FG02-93ER40795, RHIC R&D (STAR) funds, the Robert A. Welch Foundation, and the National Science Foundation through grant PHY-9511850.

References

[1] E. Gatti, P. Rehak, and J. Walton, Nucl. Instr. Meth. **226** (1984) 129.

[2] M. Clemen, T. Humanic, D. Kraus, G. Vilkelis, P. Rehak, P. Holl, E. Gatti, M. Sampietro, and J. Kemmer, Nucl. Instr. Meth. **A316** (1992) 283.

[3] R. Bellwied, R. Beuttenmueller, W. Chen, D. DiMassimo, L. Dou, H. Dyke, A. French, J. R. Hall, G. W. Hoffmann, T. Humanic, I. Kotov, H. W. Kraner, C. J. Liaw, D. Lynn, S. Paganis, L. Ray, D. Read, V. L. Rykov, S. U. Pandey, C. Pruneau, J. Schambach, J. Sedlmeir, G. Vilkelis, and W. K. Wilson., Nucl. Inst. Meth. In Press. Schloss Elmau Proceedings. 1996.

[4] P. Rehak, E. Gatti, A. Longoni, J. Kemmer, P. Holl, R. Klanner, G. Lutz, and A. Wylie, Nucl. Instr. Meth. **A235** (1985) 224.

[5] E. Gatti, A. Longoni, P. Rehak, and M. Sampietro, Nucl. Instr. Meth. **253** (1987) 393.

[6] C. Kittel, Introduction to Solid State Physics (Wiley, 5th Edition, New York 1993) p. 173.

[7] F. Seitz, Modern Theory of Solids (McGraw-Hill, New York 1940) p. 185.

[8] J. Blakemore, Modern Theory of Solids (Cambridge University Press, 2nd Edition, New York 1985) ch. 3,4.

[9] R. J. Elliot and A. F. Gibson, An Inrtoduction to Solid State Physics and its Applications (Macmillian Press Ltd, England 1974) ch. 8.

[10] E. H. Hall, Philos. Mag. **10** (1880) 301.

[11] O. Madelung and D. Meyerhofer, The physics of III/IV Compounds, John Wiley and Sons, New York 1964.

[12] F. J. Morin, Phys. Rev. **93** (1954) 62.

[13] D. Rath, Private Communication 1991.

[14] M. Clemen Private Communication.

[15] S. U. Pandey, G. Vilkelis, T. J. Humanic, H. Kraner, R. Bellwied, A. French, and J. Hall, Nucl. Instr. Meth. **361** (1995) 457.

[16] W. Press, B. Flannery, S. Teukolsky, and W. Vetterling, Numerical Recipes, Cambridge University Press, New York (1990) ch. 12,13.

[17] F. James, Comp. Phys. Comm. **20** (1980) 29.

[18] K. Seeger, Semiconductor Physics, Springer-Verlag, New York and Wien (1973) 249–259.

[19] K. Turvey and J. Dignan, Am. J. Phys. **60** (1992) 608.

[20] H. P. D. Lanyon and W. S. Neal, Physica Status Solidi A **21** (1974) 605.

[21] E. H. Putley, The Hall Effect and Related Phenomena (Butterworths, London 1960) ch. 1.

[22] W. E. Krag, Phys. Rev. **118** (1960) 435.

[23] A. F. Ioffe, Physics of Semiconductors (Academic Press Inc., New York 1960) p. 246.

[24] F. J. Morin and J. P. Maita, Phys. Rev. **96** (1954) 28.

[25] J. Messier and J. M. Flores, J. Phys. Chem. Solids **24** (1963) 1539.

[26] M. Clemen (1994) He used a similar detector at lower B fields (1 T) at the University of Pittsburgh.

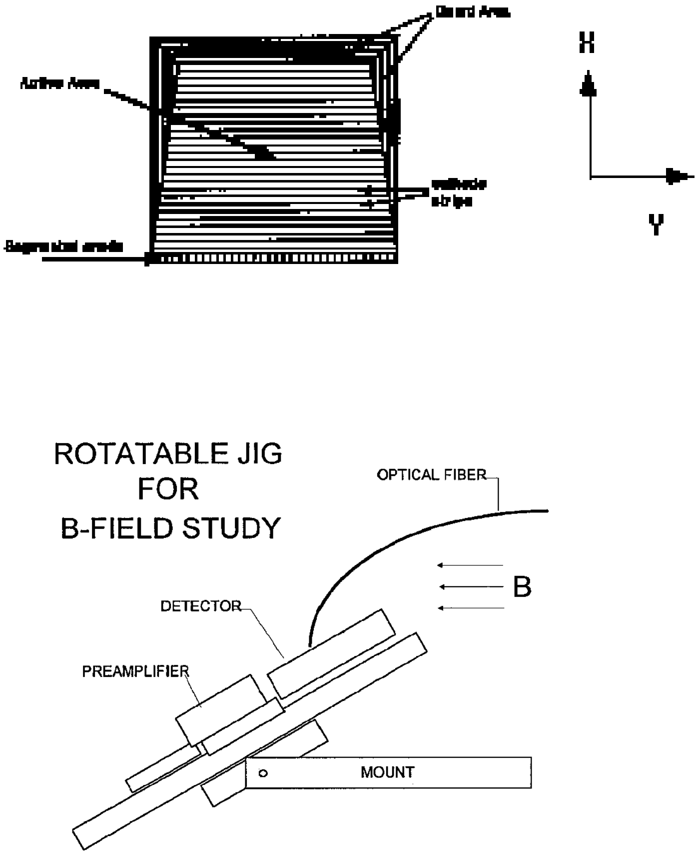

Figure 1: Schematic diagram of a STAR-1 detector and the experimental set up.

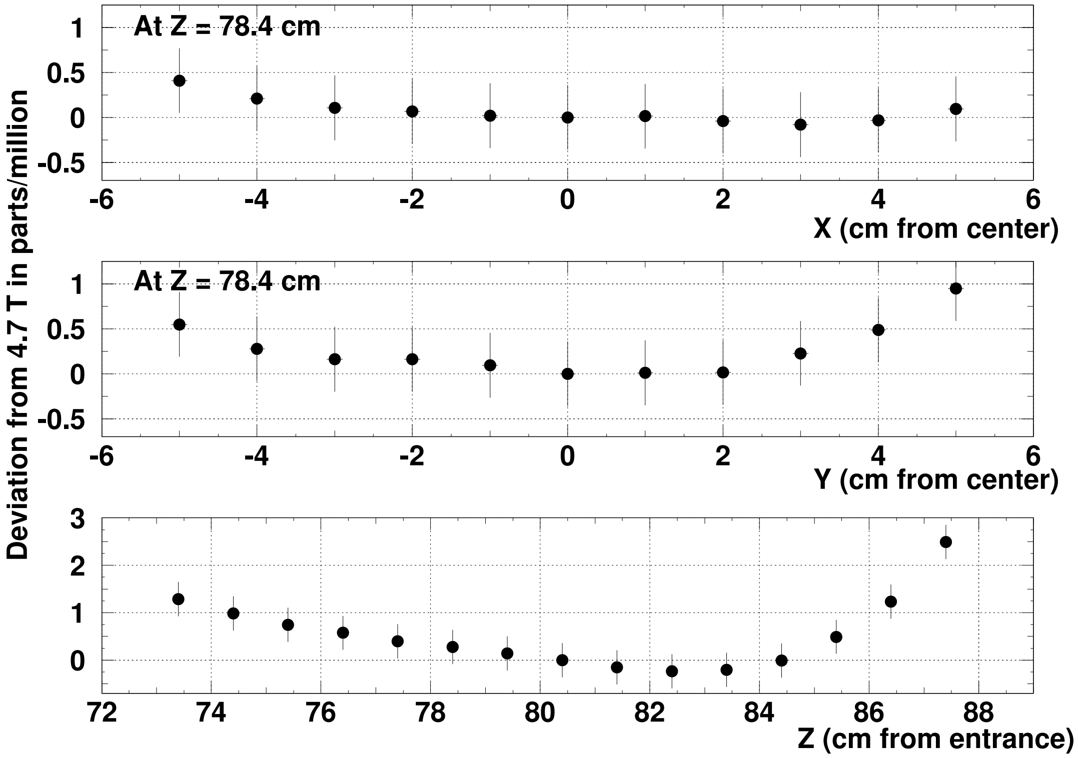

Figure 2: Profile of the magnet strength. The distances from the center of the hole within the bore are labeled by x and y. The distance from the entrance of the magnet is labeled z. The x and y measurements were not made at 80.4 cm and thus should be considered a worst case scenario.

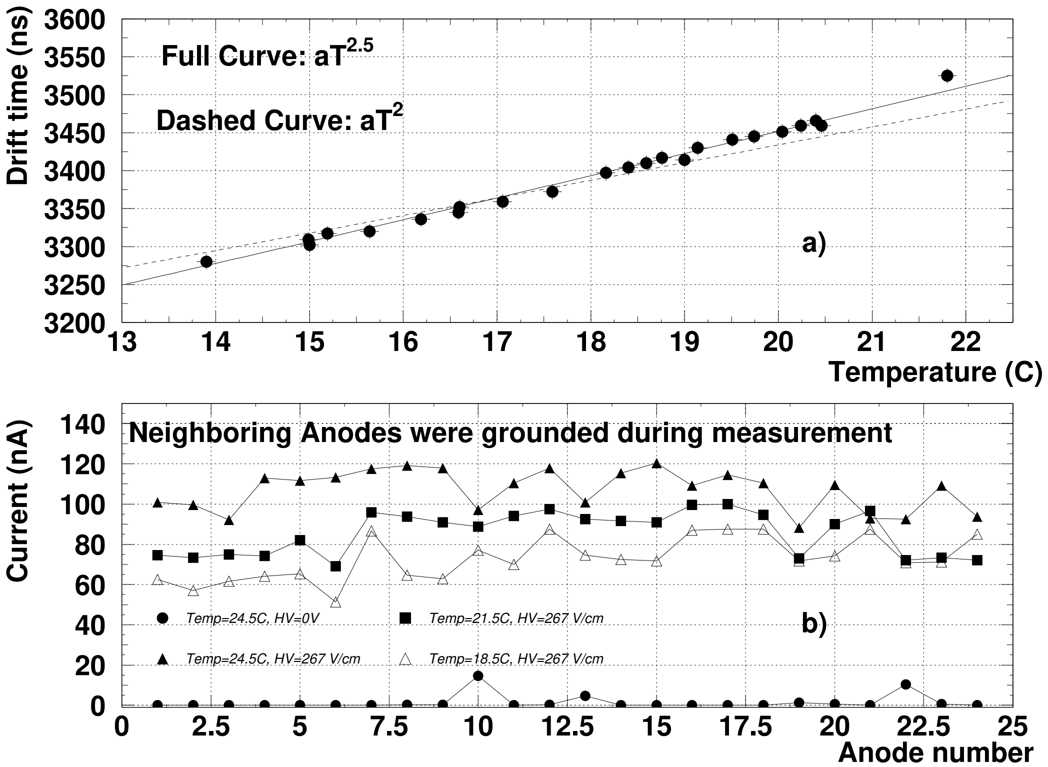

Figure 3: Temperature dependence of the detector. Note that the curve $T^{2.0}$ does not fit the data.

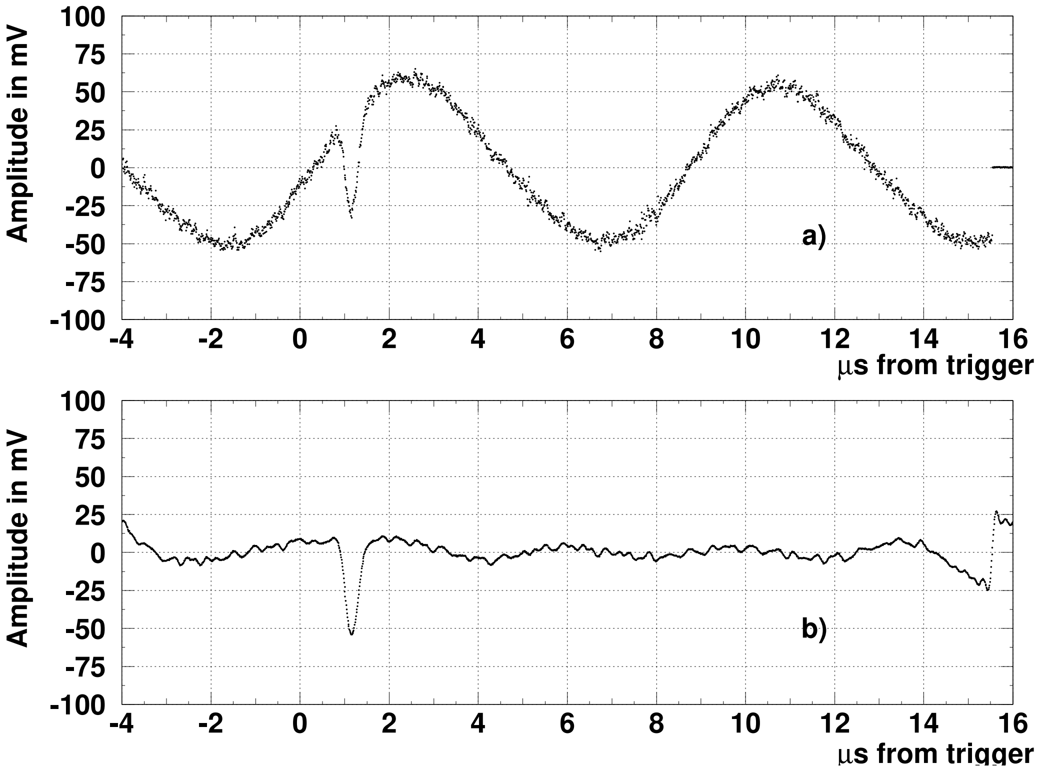

Figure 4: Fig. a shows a typical waveform taken 2.5 cm from the anodes with the detector setup in this experiment. Fig. b shows the waveform after some processing of the waveform using FFT.

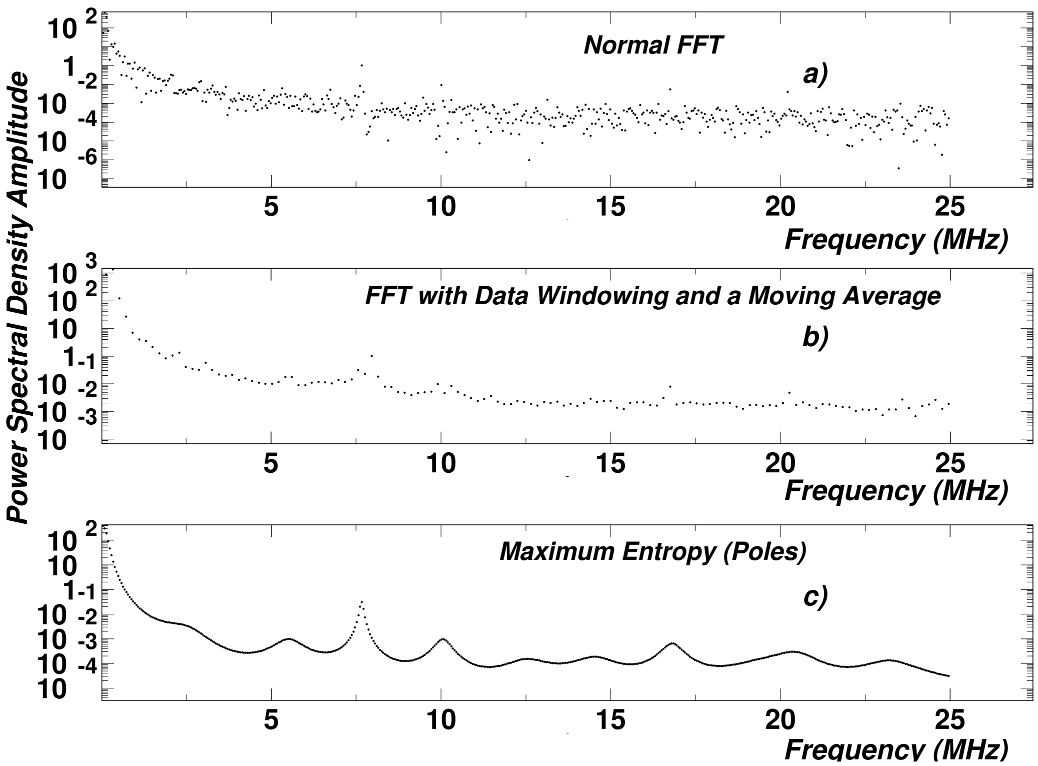

Figure 5: Estimates of the power spectral density estimates using different techniques. The maximum entropy method is best at resolving details. As an aside we mention that the peak around 8 MHz is believed to be caused by our Macintosh computer clock.

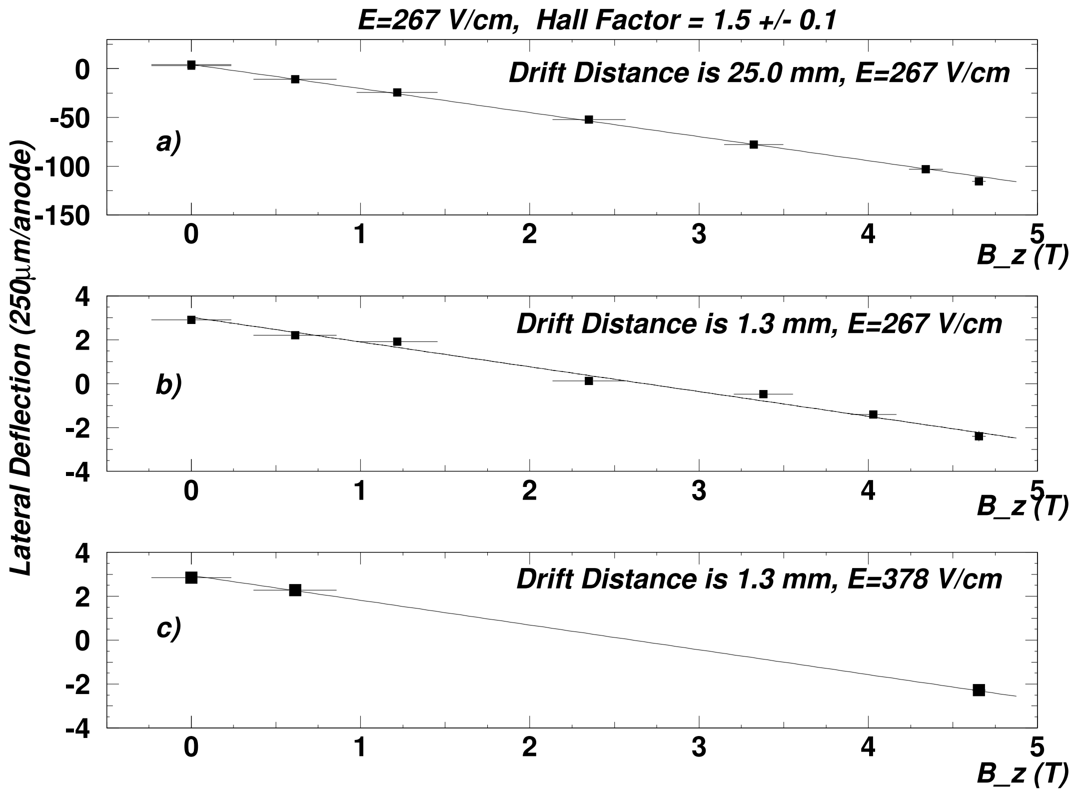

Figure 6: Lateral deflections (y) as a function of B_z for different drift fields. The lines represent eq. (3) using the same constant μ_hL for all three figures.

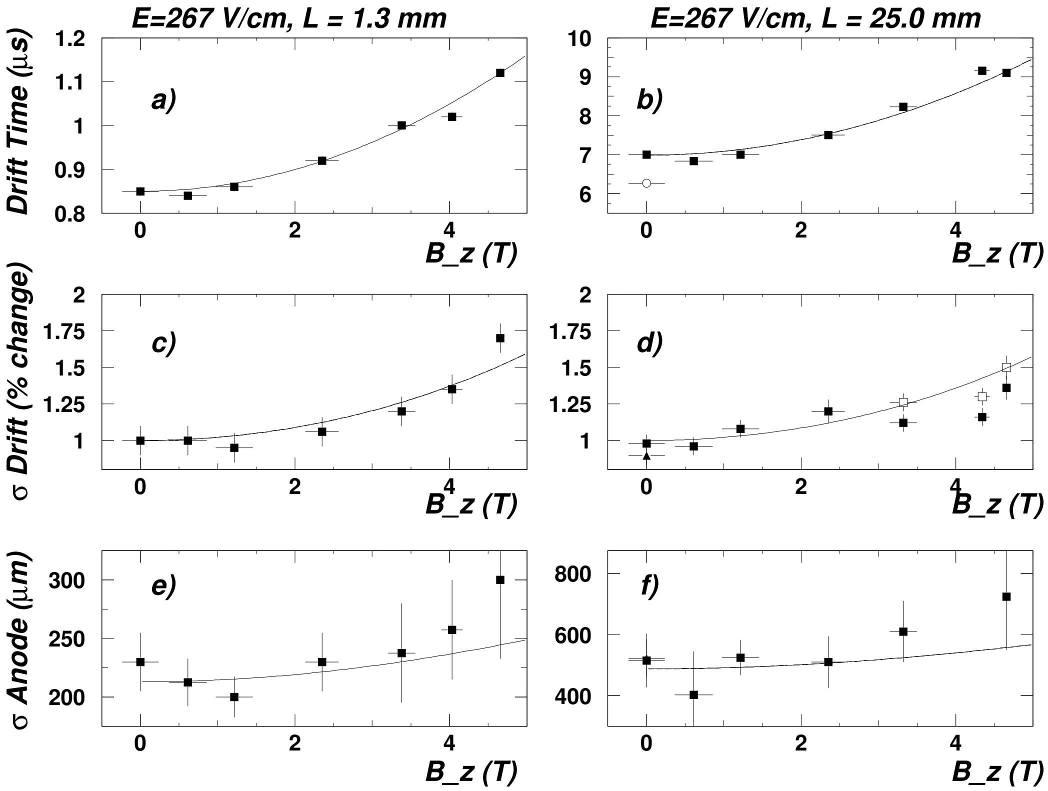

Figure 7: Drift times and cloud widths as a function of B_z for the same drift field. The plots on the left and right represent two different drift distances. The open circle in Figure 7b is for data outside the magnet. The open squares in Figure 7d arise from a renormalization of the data due to an adjustment in the laser. The lines represent eq. (6) and eq. (9) using the same drift mobility for all plots.

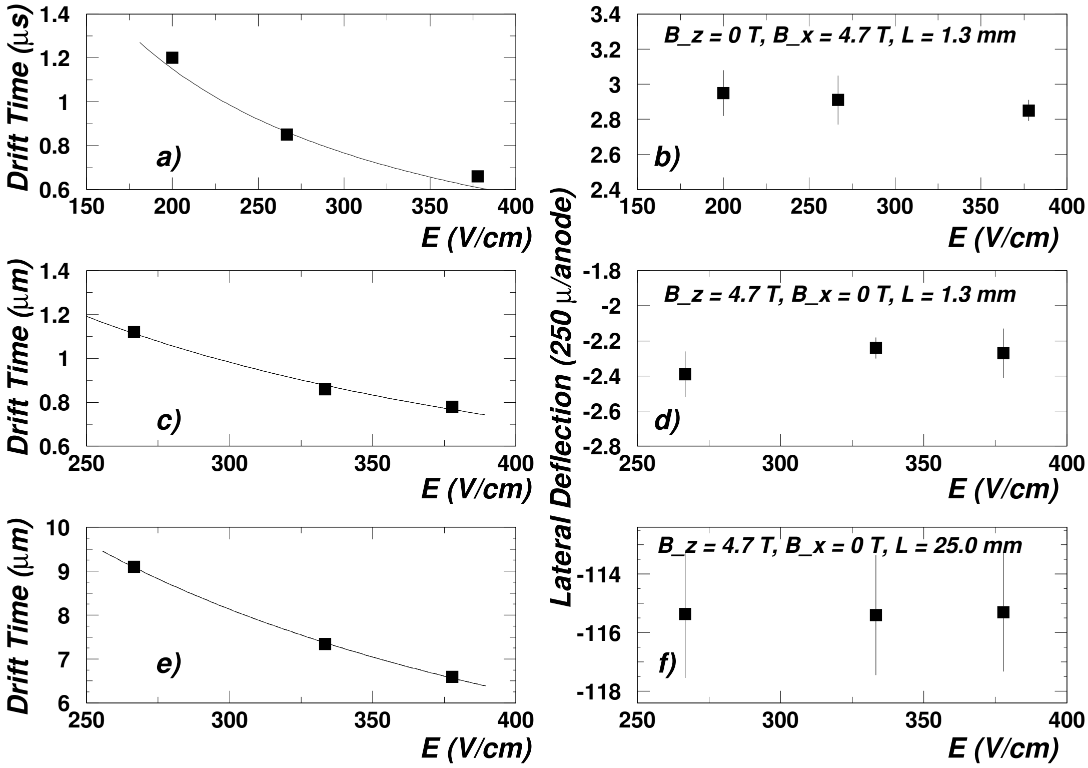

Figure 8: Drift times and lateral deflections as a function of drift field. Each pair of horizontal plots are for the same magnetic field and drift distance shown on the right. The lines in Figures 8a,c,e are fits to the 1/E dependence of the drift time to the drift field for different B fields. Figures 8b,d,f show that the transverse deflection is independent of the drift field.